Pure Appl. Geophys. 177 (2020), 5761–5780
© 2020 Springer Nature Switzerland AG, corrected publication 2020
https://doi.org/10.1007/s00024-020-02606-w

Pure and Applied Geophysics

The Importance of Atmospheric Corrections on InSAR Surveys Over Turkey: Case Study of Tectonic Deformation of Bodrum-Kos Earthquake

Fikret Dogru[1]

Abstract—The Bodrum-Kos earthquake which occurred on 20th July 2017 at 1:31 am local time with a magnitude of Mw 6.6 in the Gulf of Gökova in Turkey. The Bodrum-Kos earthquake caused a small radius tsunami in Bodrum coast and its surroundings. Here, the Interferometric Synthetic Aperture Radar (InSAR) method was utilized to reveal tectonic deformation caused by the Bodrum-Kos earthquake. The InSAR technique was increasingly used to detect ground deformation such as landslide, tectonic or volcanic. In this study, the crucial atmospheric corrections which are GACOS and phase-elevation corrections on InSAR data are discussed. GACOS correction is based on high-resolution European Centre for Medium-Range Weather Forecasts weather model at 0.125° and 6-h resolutions, SRTM DEM and ASTER GDEM. GACOS is used to separate stratified and turbulent signals from tropospheric total delays and generate high spatial resolution zenith total delay maps to be used for correcting InSAR measurements and other applications. Phase-elevation linear correction is also used to separate mostly stratified signals from tropospheric total delays due to the topographic elevation changes and 3 arc second topographic map was used in the phase-elevation correction. These atmospheric correction methods were tried both separately and sequentially and standard deviations of each method were presented. The points comparison of the cumulative line of sight displacement maps were made after and before correction. The point on the Karaada (C point) shows subsidence after the earthquake and then recovers again. Time-series results of all points show similar values until the earthquake occurs. Time-series result also shows that the Bodrum-Kos earthquake has a small radius effect over the land area only the north and maybe west island due to the occurrence on the sea and lost its much energy without reaching the land.

Keywords: GACOS, InSAR, phase-elevation, Bodrum-kos, earthquake, Karaada.

1. Introduction

The Gulf of Gökova which is located in the western part of Turkey has gained its current form by the help of the collision of Anatolian, African and Eurasian plates so this process formed Western Anatolia Extension Province (WAEP) system. Moreover, WAEP caused to occur Gediz, Buyuk and Kucuk Menderes Graben systems and west to east directional active faults (Sengor et al. 1984). The extension in the Western Anatolia causes a large number of historic earthquakes (Mw $>$ 5) in the Gulf of Gökova. Different models were recommended for the extension as four type models which are Anatolian plate escape, orogenic collapse, back-arc extension and the combined model of the three models (Dewey 1988; Seyitoğlu and Scott 1991; Dewey and Şengör 1979; Le Pichon and Angelier 1979).

Radar interferometry (InSAR) has been used to reveal ground deformation resulting from especially bigger than Mw 6.0 earthquakes successfully. Several researchers use InSAR data to determine tectonic deformation: Simons et al. (2002) used InSAR method to investigate co-seismic deformation due to the Hector Mine earthquake which occurred in the eastern California shear zone with a moment magnitude (Mw) of 7.1 in 1999. Chlieh et al. (2004) examined the Antofagasta earthquake that occurred in Chile in 1995 with Mw 8.1 with GPS and InSAR method to detect co-seismic deformation. Wright et al. (2004) used InSAR method to obtain 3D displacement maps for the Nenana Mountain Earthquake that occurred on 23 October 2002 in Alaska with Mw $\sim$ 6.7. Biggs et al. (2006) carried out an InSAR

The original version of this article was revised: reference Albino et al. 2020 has been omitted.

[1] Oltu Vocational College, Construction Technology, Ataturk University, Erzurum, Turkey. E-mail: fikretjfm@gmail.com

study to investigate 1994 Mw 6.0 and 2004 Mw 6.5 Al Hoceima earthquakes in Morocco. Biggs et al. (2009a, b) studied postseismic deformation resulting from 2002 Denali Fault earthquake in Alaska with InSAR data between 2003 and 2005 period and investigated 2007 Pisco earthquake in Peru to identify 3D ground displacement map. Motagh et al. (2010) investigated the source fault of the Tocopilla earthquake that occurred in Chile on 14 November 2017 with Mw 7.8, slip distribution and fault interaction by combining aftershock locations, satellite interferometry data and stress model simulations. Hooper et al. (2018) suggested Centre for the Observation and Modelling of Earthquakes, Volcanoes and Tectonics (COMET) which responds volcanic and significant tectonic deformations (Mw $\geq$ 6.0). Albino et al. (2019) studied the Agung and Batur volcano area to investigate volcanic-tectonic deformation with InSAR data.

Moreover, several researchers have made studies on Turkey with InSAR data to reveal ground deformation resulting from earthquakes: Burgmann et al. (2002) used 50 Global Positioning System (GPS) sites with InSAR method to determine the geometry and slip distribution of the coseismic rupture because of Düzce earthquake which occurred on 12 November 1999 at 18:57:22 local time with Mw 7.2. Kaneko et al. (2013) carried out an InSAR study over the North Anatolian Fault (NAF) in Turkey to obtain interseismic deformation. Also, 1999 Izmit earthquake with Mw 7.4 was investigated using InSAR method by Delouis et al. (2000), Reilinger et al. (2000), Wright et al. (2001), Michel et al. (2002), Bos et al. (2004), Hamiel and Fialko (2007) and Ergintav et al. (2009). 23 October 2011 Van earthquake (Mw 7.2) was studied using InSAR data by Dogan et al. (2014), Elliott et al. (2013), Fielding et al. (2013), Feng et al. (2014) and Wang et al. (2015).

In this paper, displacement resulting from 20 July 2017 Bodrum-Kos earthquake in the Bodrum and Karaada was investigated using InSAR data and atmospheric effects were removed from interferograms before inversion. Then, the cumulative line of sight (LOS) displacement comparison of four points from different areas and all the pixel values of Karaada were made before and after correction. In addition, InSAR studies were carried out by Karasözen et al. (2018), Tiryakioğlu et al. (2018), Ganas et al. (2018), Cordrie et al. (2018) and Konca et al. (2019). In this study, the production of corrected InSAR time series on Bodrum-Kos earthquake will be focused on using Sentinel-1 dataset. The quality of the atmospheric corrections will be compared using the last weather models products (e.g. high-resolution ECMWF) with the ones obtained with the simple phase-elevation method.

2. Data and Methodology

2.1. Sentinel-1 Data

Sentinel-1A and Sentinel-1B satellites were launched under the European Union's Earth Observation program in 2014 and 2016 respectively. An installation of satellites is consisting of two conjugate satellites with a C band of ESA. The C band SAR imaging task of European Space Agency (ESA)'s ERS and Envisat satellites continues with this new set of satellites. The frequency of imaging was increased by two satellites in the same orbit and the temporal resolution was reported as 6-day exact repeat cycle at the equator, but the revisit rate is significantly greater at higher latitudes than at the equator.

In this study, interferograms that are generated from Sentinel-1 data are used with the help of COMET-LiCS Sentinel-1 InSAR portal project (Gonzales et al. 2016). These interferograms are processed with GAMMA software (Werner et al. 2000) and the resolutions of interferograms are $\sim$ 90 m. The corrections are applied on 135 interferograms (ascending + descending) which were produced using the COMET LiCSAR service (https://comet.nerc.ac.uk/COMET-LiCS-portal/) (Lawrence et al. 2013; González et al. 2016; Morishita et al. 2020).

2.2. Atmospheric Corrections

Phase delays may take place by reason of changes in water vapour, pressure and temperature in the troposphere between acquisitions that consist of a "stratified" component, which is associated with vertical stratification of atmospheric properties and hereby correlates with the topography and a

"turbulent" component, which is spatially correlated over short wavelengths. Besides, Generic Atmospheric Correction Online Service for InSAR (GACOS) correction which is based on the European Centre for Medium-Range Weather Forecasts (ECMWF) weather model (Doin et al. 2009; Jolivet et al. 2011) at 0.125° and 6-h resolutions, SRTM DEM (90 m, S60-N60), ASTER GDEM (90 m, N60-N83, S60-S83).

In this study, GACOS which is provided by Newcastle University (Yu et al. 2017, 2018a, b) is used to separate stratified and turbulent signals from tropospheric total delays and generate high spatial resolution zenith total delay maps was used for correcting InSAR measurements and other applications. Phase-elevation correction is also used to mostly stratified due to the topographic elevation changes and 3 arc second topographic map of 90-m Digital Elevation Model (DEM) provided by the Shuttle Radar Topographic Mission (SRTM) was used in the phase-elevation correction.

2.3. Quality Assessment of Atmospheric Corrections

To check the quality of atmospheric corrections, the relative difference of standard deviation of interferograms were calculated before and after correction, using the following formula:

$$Q = \frac{\sigma_i - \sigma_c}{\sigma_i} \times 100 \tag{1}$$

where σ_i is the standard deviation of uncorrected interferogram and σ_c is the standard deviation of corrected interferograms. The quality of GACOS, the phase-elevation and combined method which includes GACOS, detrend and phase-elevation corrections were tested (Albino et al. 2020).

2.4. A Least Square Inversion Method

A least-squares inversion method was performed on corrected interferograms to obtain time series of ground change. The ground displacements m at each SAR acquisition can be related to the InSAR data I according to

$$Gm = I \tag{2}$$

The data vector I contain the ground change observation at a given pixel location (i, j), for all interferograms. The design matrix, G, is constructed from the temporal distribution of SAR scene acquisitions. Assume that the InSAR data set consists of M interferograms from N independent SAR scenes. The dates of the SAR scenes are contained in chronological order in the 1 × N vector S. H is a 2 × M matrix containing the beginning and ending date for each interferogram ordered by the date of the first scene. The incremental range change and the InSAR data are related through a combination of ones and minus ones using the information in H and L,

$$G_{ij} = \left\{ \begin{array}{cc} 1 & for\ S_i = H_{i1} \\ -1 & for\ S_i = H_{i2} \end{array} \right\} \tag{3}$$

In this study, M = 78 is the number of ascending interferograms and N = 29 is the number of SAR scenes and M = 57 is the number of descending interferograms and N = 23 is the number of SAR scenes were used for inversion stage (Usai 2003; Le Mouélic et al. 2005).

2.5. The Line of Sight (LOS) Velocity Calculation

Moreover, a weighted averaging method was used which optimizes the contribution of interferograms in terms of signal to noise ratio. In this approach, the estimated LOS velocity rate is obtained by a least-squares optimization. Assuming that the temporal evolution of the displacement is a constant V, the estimated value $\widehat{V}$ is given by,

$$\widehat{V} = \left(\sum_{i=0}^{M-1} \Delta t_i \times \Delta h_i \right) / \left(\sum_{i=0}^{M-1} {\Delta t_i}^2 \right) \tag{4}$$

where Δt_i is the time span of interferograms and Δh_i is the corrected LOS phase values (Le Mouélic et al. 2005).

2.6. Calculation of Horizontal and Vertical Displacement Components

Line of Sight displacement d_{LOS} that is obtained from the InSAR technique is the projection of 3D displacement and contains east (d_e), up (d_u) and north

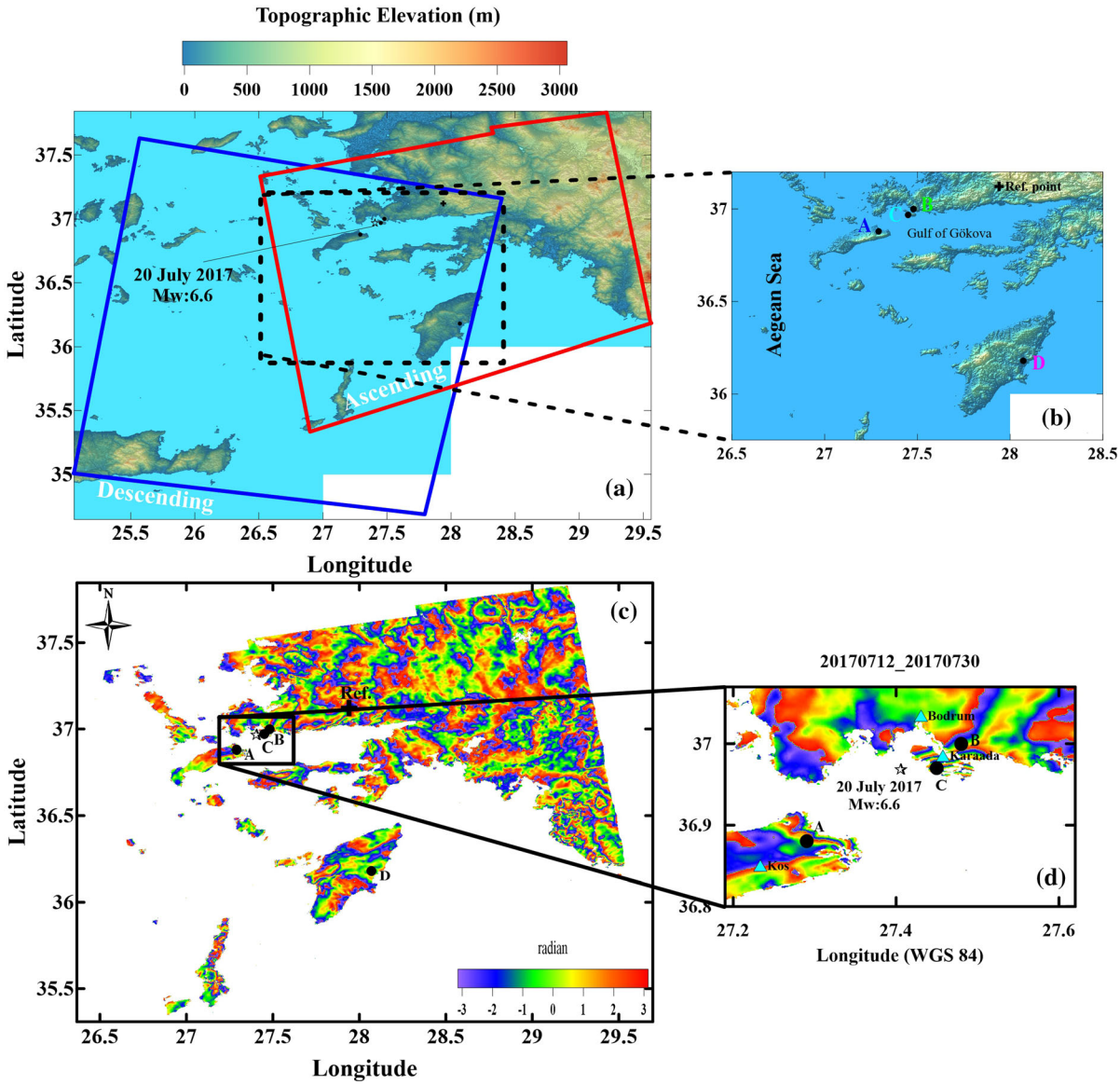

Figure 1

a Topographic elevation of the study area with ascending and descending frames, **b** zoomed to black dashed area in order to show A, B, C, D and reference point **c** 12–30th July 2017 interferogram showing the reference point (Ref.) used for atmospheric corrections and the four points A, B, C and D used for the time series. **d** the visible deformation fringes on the island with the black star showing the earthquake epicentre

(d_n) displacement components into the LOS direction. d_{LOS} is given by (Hanssen 2001),

$$d_{LOS} = d_u \times cos(\theta_{inc}) - d_{ALD} \times sin(inc) \quad (5)$$

where d_{ALD} is the projection of the multiple horizontal components on the azimuth look direction (ALD) and is given by (Hanssen 2001),

$$d_{ALD} = d_e \times cos(\alpha_h) - d_n \times sin(\alpha_h) \quad (6)$$

where θ_{inc} is the incidence angle and change between 30° and 46° for ascending and descending. Incidence angles of each point are used in this study. α_h is the heading (azimuth) angle 350° for ascending and 190° for descending. It is thought that InSAR studies are not sensitive to d_n component due to satellite trajectory so d_n component is omitted d_e and d_u components are calculated.

Table 1

Time acquisitions of GACOS corrections

Ascending		Descending	
20170501	20170730	20170501	20170817
20170505	20170805	20170507	20170829
20170513	20170811	20170513	20170916
20170519	20170817	20170519	20170922
20170525	20170823	20170525	20170928
20170531	20170829	20170531	20171004
20170606	20170904	20170606	20171010
20170612	20170910	20170612	20171022
20170618	20170916	20170618	
20170624	20170922	20170624	
20170630	20170928	20170630	
20170706	20171004	20170706	
20170712	20171010	20170712	
20170718	20171016	20170718	
20170724		20170724	

3. Tectonic Deformation

3.1. 20 July 2017 Bodrum-Kos Earthquake

In order to determine the tectonic deformation which was revealed after Bodrum-Kos earthquake, the ascending and descending interferograms between May to October 2017 were used. This study was carried out using a total of 135 interferograms. Figure 1 shows the phase difference map of the test area and the formed fringes can be seen on the northern island by zooming the earthquake area with a topography map of the study area. Topography values reach up to 3000 m over the southeastern part of the study area. The earthquake occurred in Gökova Bay at 36.9620 N and 27.4053 E [Kandilli Observatory and Earthquake Research Institute (KOERI)] on July 20, 2017, at 1:31 am local time with a magnitude of Mw = 6.6 (Ml = 6.2) at 5 km depth and caused a small tsunami on the coast of Bodrum. The National Observatory of Athens reports that the earthquake occurred at 36.9643 N and 27.4332 E coordinates with a magnitude of Mw = 6.4 (Ml = 6.2) at a depth of 10.2 km. Fault mechanism calculations show that the earthquake is caused by normal faulting and causes many aftershocks that reach the highest magnitude Mw = 4.8 after the mainshock. Therefore, 78 ascending and 57 descending interferograms were processed to evaluate the tectonic deformation and 29 and 23 times of acquisitions for ascending and descending respectively GACOS corrections were

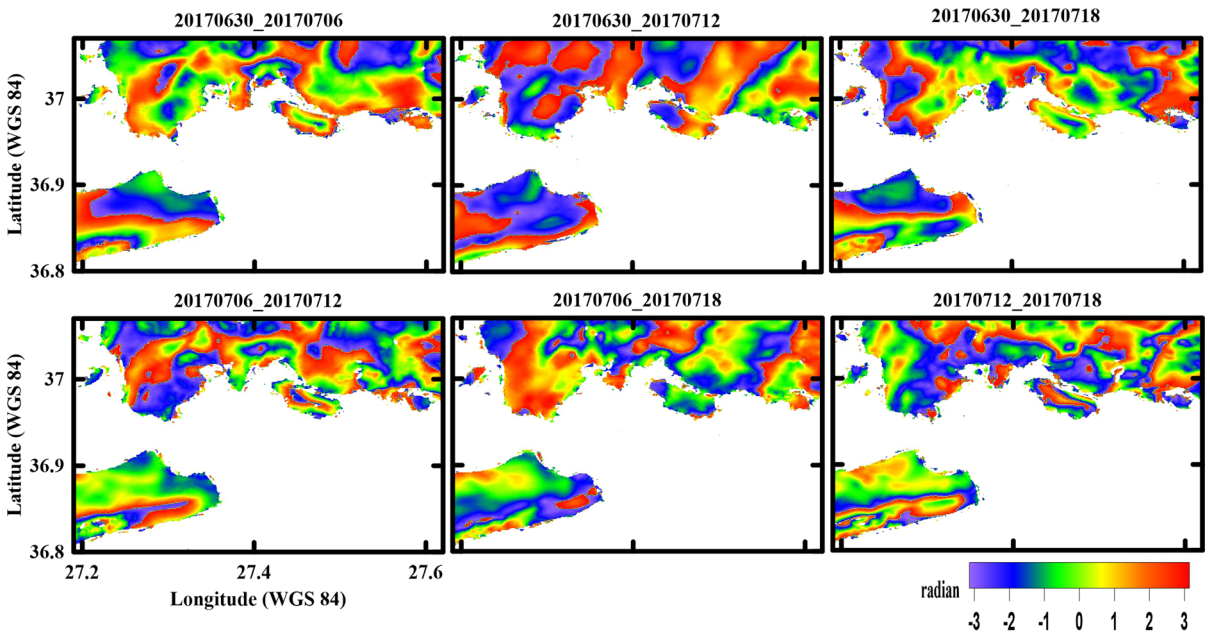

Figure 2
Ascending interferograms between 30th June–6th July 2017 and 12–18th July 2017 before the earthquake

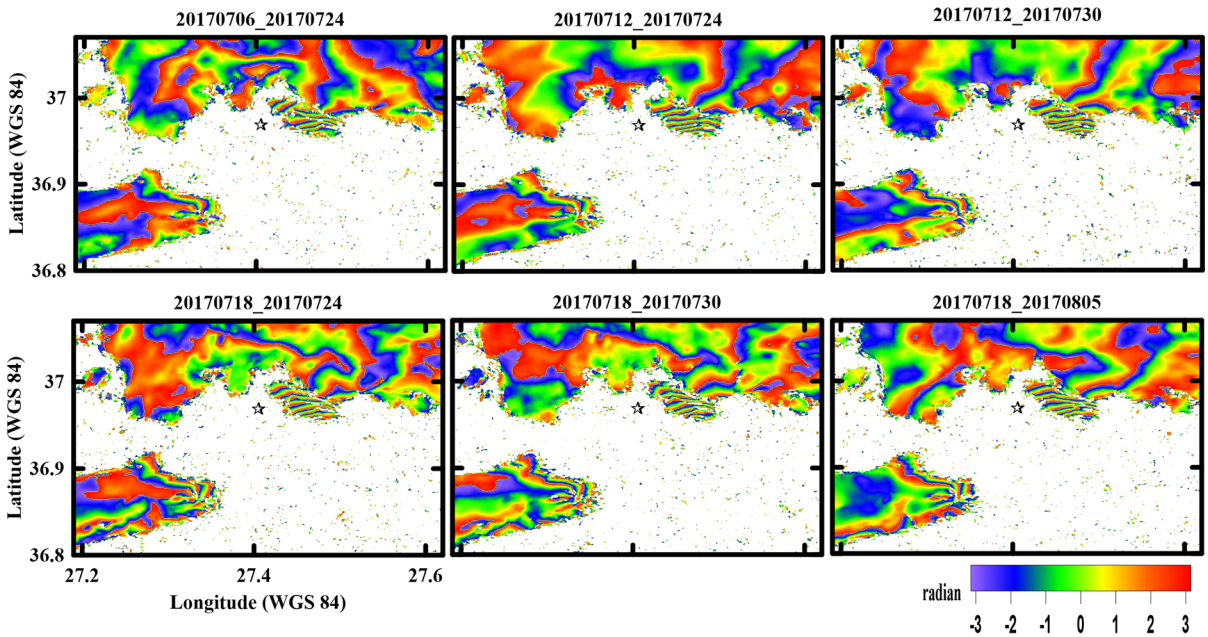

Figure 3
Ascending interferograms between 6–24th July 2017 and 18th July–5th August 2017, the earthquake occurred between these dates and the black star indicates the earthquake epicentre

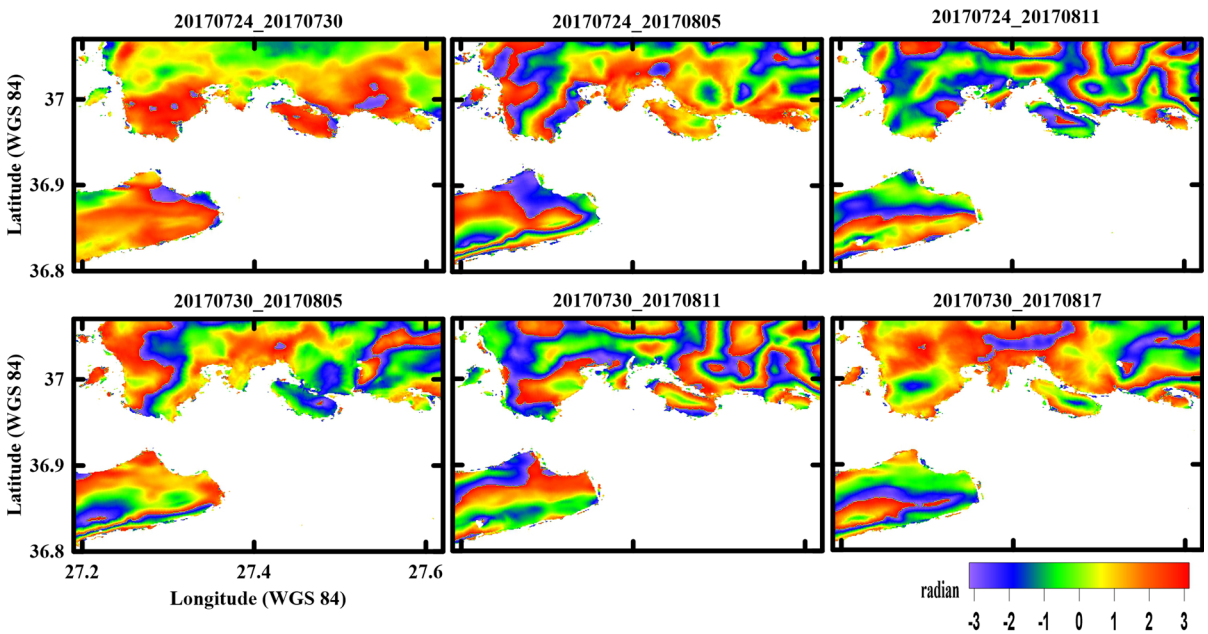

Figure 4
Ascending interferograms between 24–30th July 2017 and 30th July–17th August 2017 after the earthquake

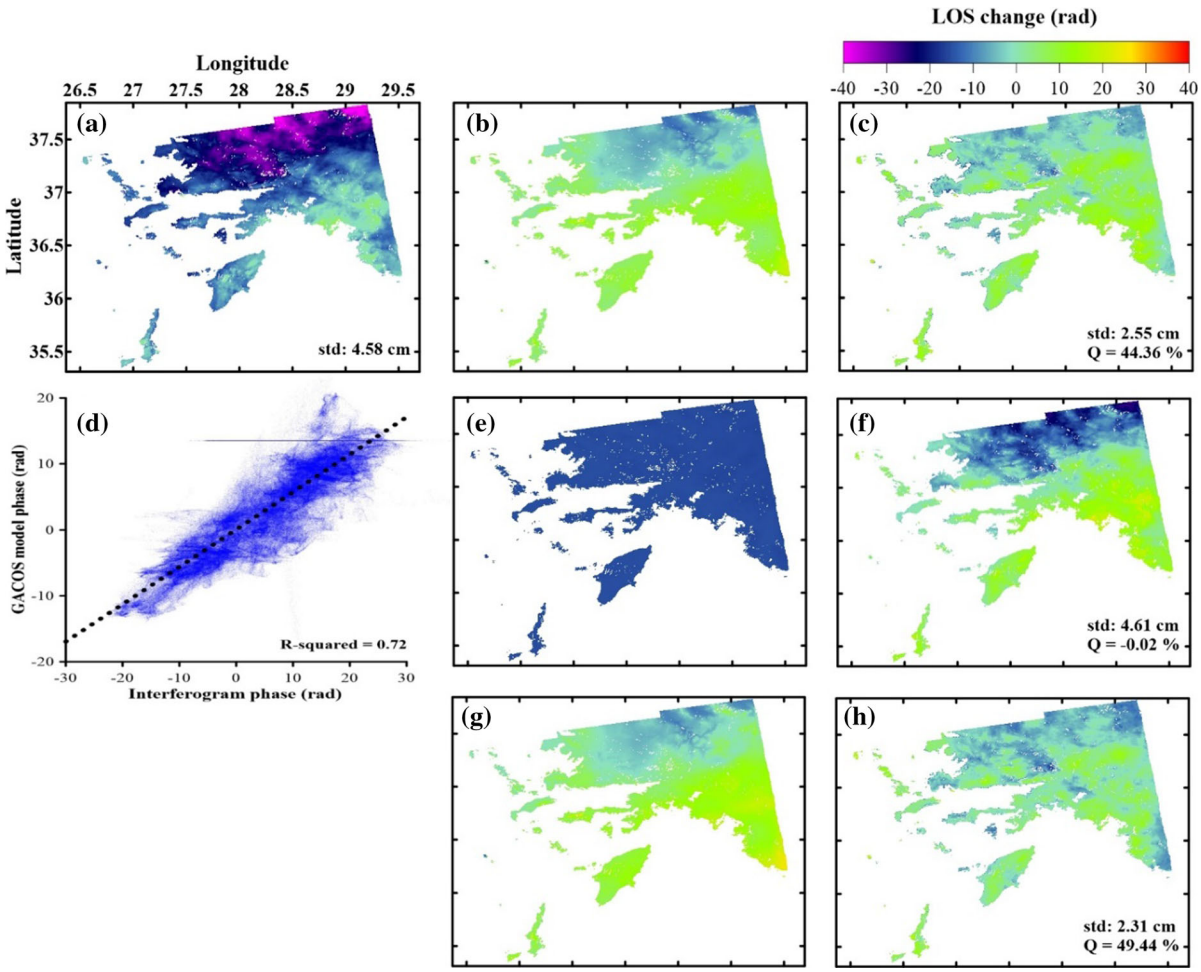

Figure 5

Atmospheric correction result of 18–30 July 2017 ascending interferogram **a** uncorrected interferogram showing a strong negative LOS change over the North part of study area, **b** atmospheric phase delay maps based on GACOS weather-model, **c** residual phase delay map after GACOS correction, **d** uncorrected interferogram and GACOS weather-model phase correlation, **e** atmospheric phase delay maps based on phase-elevation correlation, **f** residual phase delay map after phase-elevation correction, **g** combination delay maps of GACOS, phase-elevation method and detrend method to eliminate linear ramp, **h** residual phase delay map after combined method

requested from Newcastle University between May and October 2017 (Table 1).

To show deformation fringes which were seen after the earthquake, the unwrapped interferograms were presented between the dates before and after the earthquake with pre and post unwrapped interferograms. In the post-earthquake analyses, deformation fringes were not found in phase difference maps in Fig. 2. The time span of the master and slave pair does not include the earthquake date so deformation fringes could not be observed in these maps. But, when the dates between 6 July—24 July 2017 and 18 July—5 August 2017 interval are examined, the deformation fringes can easily be observed in the north island of earthquake epicentre (Fig. 3). Also, the post-earthquake difference maps were examined and deformation fringes were not recognized in Fig. 4.

Figure 5a shows the ascending interferogram 18–30th July 2017 which has an overall standard deviation of 4.58 cm. The atmospheric signal consists of high negative LOS changes of 40 rad around the north part of the interferogram. The R-square value of the correlation between the interferogram phase and

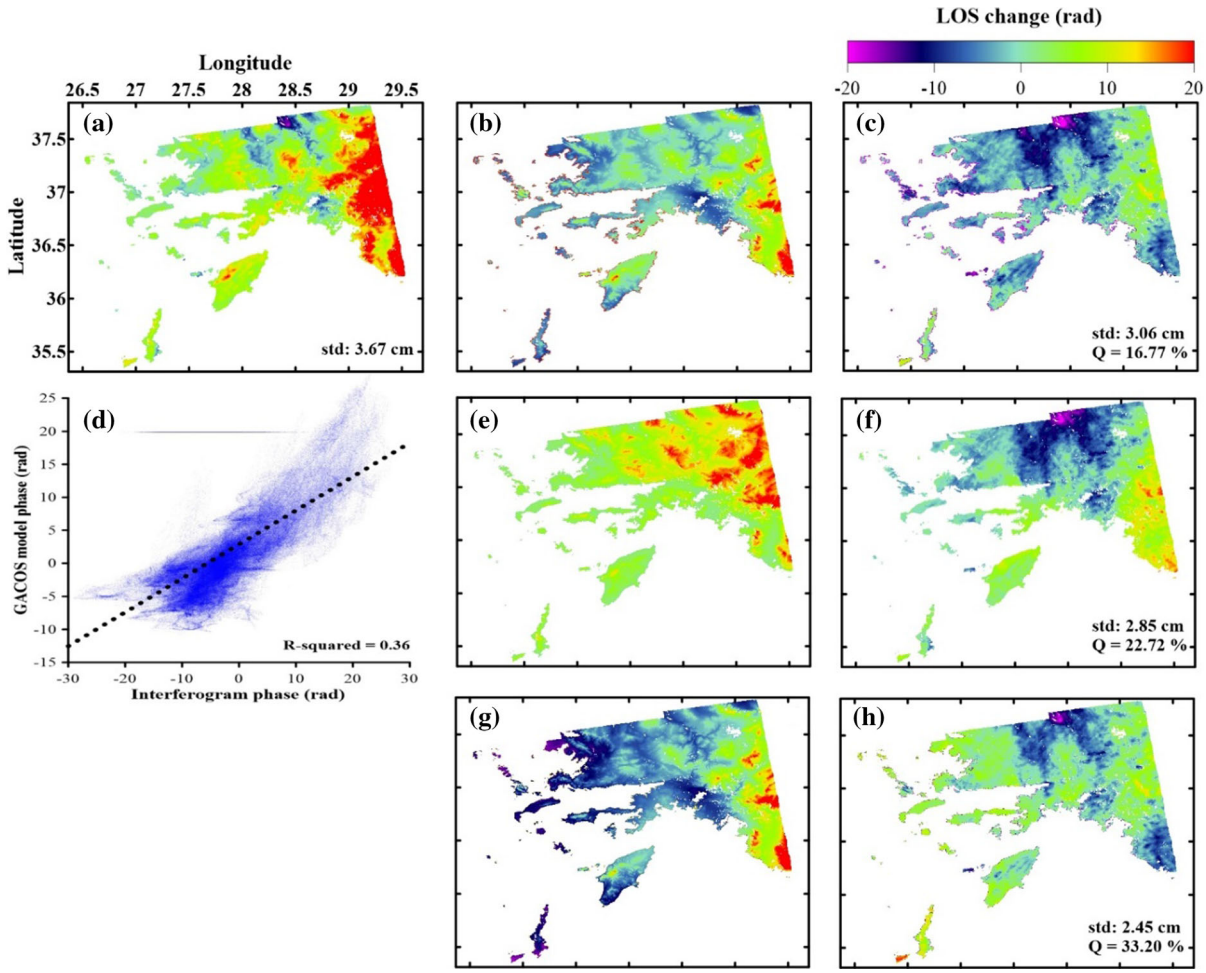

Figure 6

Atmospheric correction result of 18–30 June 2017 ascending interferogram **a** uncorrected interferogram showing a strong positive LOS change over the eastern part, **b** atmospheric phase delay maps based on GACOS weather-model, **c** residual phase delay map after GACOS correction, **d** uncorrected interferogram and GACOS weather-model phase correlation, **e** atmospheric phase delay maps based on phase-elevation correlation, **f** residual phase delay map after phase-elevation correction, **g** combination delay maps of GACOS, phase-elevation method and detrend method to eliminate linear ramp, **h** residual phase delay map after combined method

GACOS weather-model phase is 0.72 in Fig. 5d. Therefore, GACOS weather-model in Fig. 5b is corrected the high atmospheric signals in 18–30th July 2017 interferogram with the 44.36% quality and reduced the standard deviation as 2.55 cm in Fig. 5c. Also, phase-elevation linear model in Fig. 5e consists of negative signals for the whole area so the phase-elevation linear model could not correct the interferogram and the standard deviation is obtained as 4.61 cm in Fig. 5f. The combine method phase in Fig. 5g helps to reduce the standard deviation of 2.31 cm with the 49.44% quality in Fig. 5h.

Figure 6a shows the ascending interferogram 18–30th June 2017 which has an overall standard deviation of 3.67 cm. The atmospheric signal consists of high positive LOS changes of 20 rad around the east part of the interferogram. The R-square value of the correlation between the interferogram phase and GACOS weather-model phase is 0.36 in Fig. 6d. Therefore, GACOS weather-model in Fig. 5b is corrected the high atmospheric signals in 18–30th June 2017 interferogram with the 16.77% quality and reduced the standard deviation of 3.06 cm in Fig. 6c. Also, phase-elevation linear model in Fig. 6e is

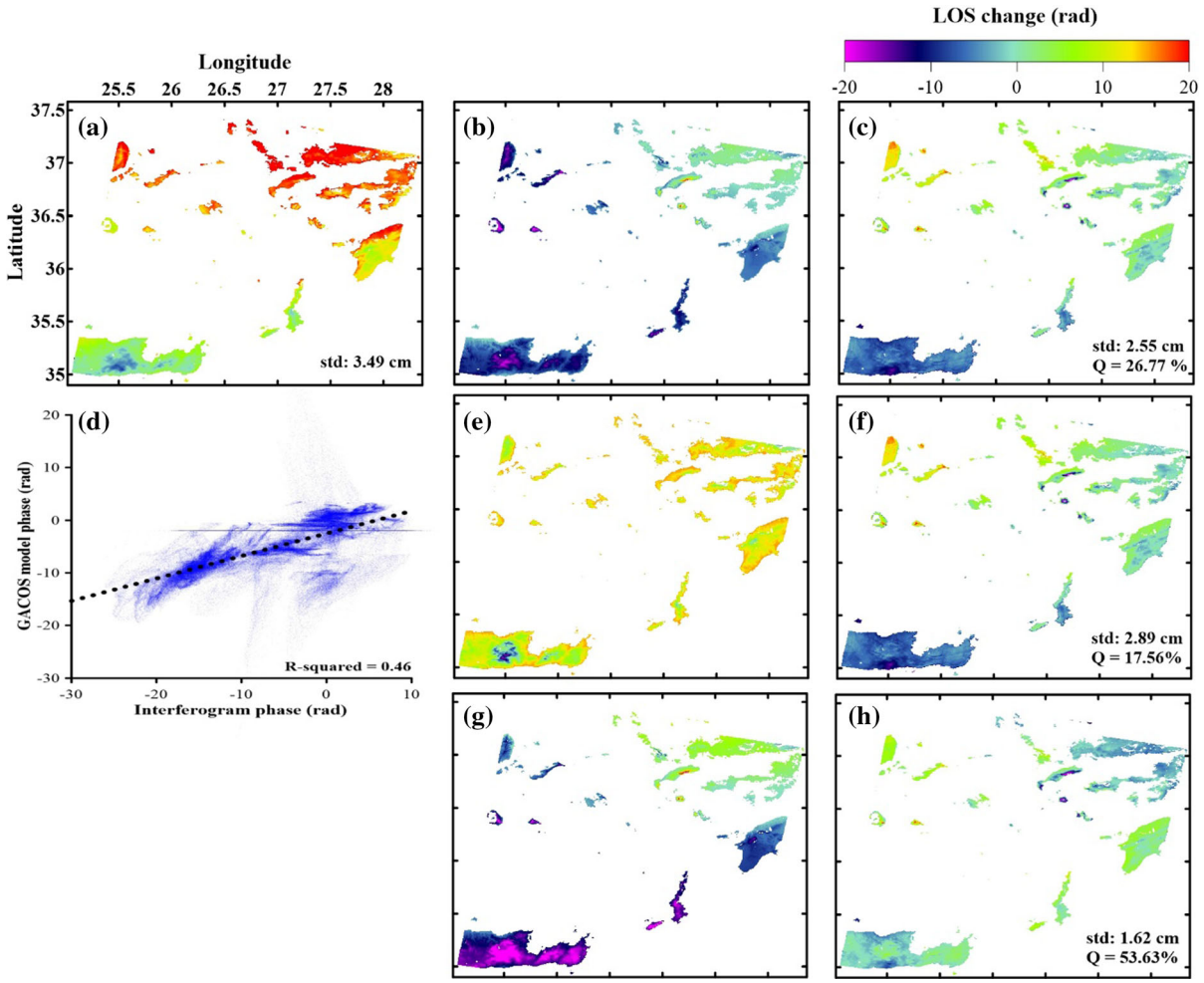

Figure 7

Atmospheric correction result of 13–31 May 2017 descending interferogram **a** uncorrected interferogram showing a strong positive LOS change over the North part, **b** atmospheric phase delay maps based on GACOS weather-model, **c** residual phase delay map after GACOS correction, **d** uncorrected interferogram and GACOS weather-model phase correlation, **e** atmospheric phase delay maps based on phase-elevation correlation, **f** residual phase delay map after phase-elevation correction, **g** combination delay maps of GACOS, phase-elevation method and detrend method to eliminate linear ramp, **h** residual phase delay map after combined method

corrected high signals over the eastern part with the 22.72% quality and reduced the standard deviation of 2.85 cm in Fig. 6f. The combine method phase in Fig. 6g helps to reduce the standard deviation of 2.45 cm with the 33.20% quality in Fig. 6h.

Figure 7a shows the descending interferogram 13–31th May 2017 which has an overall standard deviation of 3.49 cm. The atmospheric signal consists of high positive LOS changes of 20 rad most of the interferogram. The R-square value of the correlation between the interferogram phase and GACOS weather-model phase is 0.46 in Fig. 7d. Therefore, GACOS weather-model in Fig. 7b is corrected the high atmospheric signals in 13–31th May 2017 interferogram with the 26.77% quality and reduced the standard deviation of 2.55 cm in Fig. 7c. Also, phase-elevation linear model in Fig. 7e is corrected high signals most of the interferogram with the 17.56% quality and reduced the standard deviation of 2.89 cm in Fig. 7f. The combine method phase in Fig. 7g helps to reduce the standard deviation of 1.62 cm with the 53.63% quality in Fig. 7h.

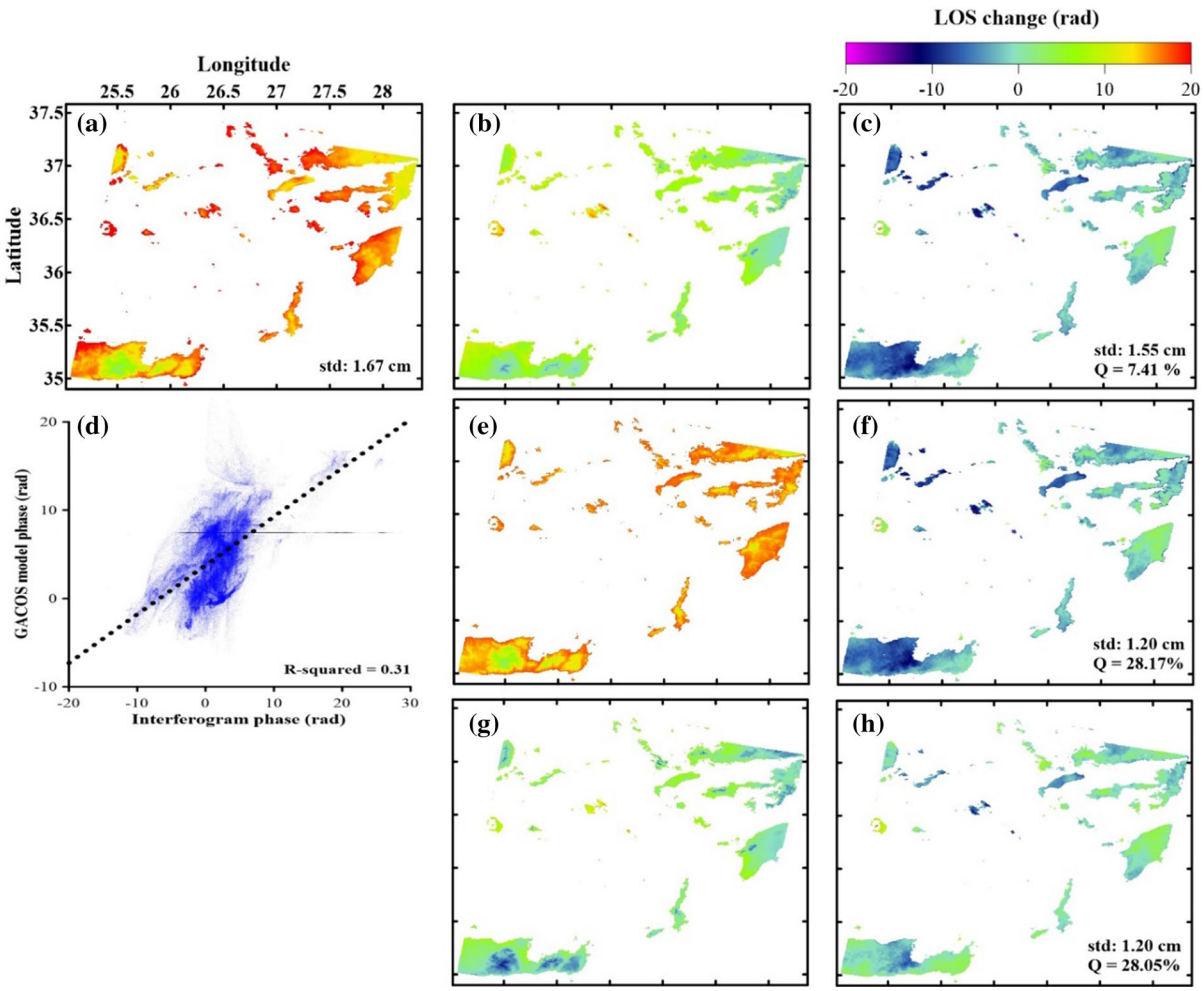

Figure 8

Atmospheric correction result of 13–25 May 2017 descending interferogram **a** uncorrected interferogram showing a strong positive LOS change almost all area, **b** atmospheric phase delay maps based on GACOS weather-model, **c** residual phase delay map after GACOS correction, **d** uncorrected interferogram and GACOS weather-model phase correlation, **e** atmospheric phase delay maps based on phase-elevation correlation, **f** residual phase delay map after phase-elevation correction, **g** combination delay maps of GACOS, phase-elevation method and detrend method to eliminate linear ramp, **h** residual phase delay map after combined method

Figure 8a shows the descending interferogram 13–25th May 2017 which has an overall standard deviation of 1.67 cm. The atmospheric signal consists of high positive LOS changes of 20 rad most of the interferogram. The R-square value of the correlation between the interferogram phase and GACOS weather-model phase is 0.31 in Fig. 8d. Therefore, GACOS weather-model in Fig. 8b is corrected the high atmospheric signals in 13–25th May 2017 interferogram with the 7.41% quality and reduced the standard deviation of 1.55 cm in Fig. 8c. Also, phase-elevation linear model in Fig. 8e is corrected high signals most of the interferogram with the 28.17% quality and reduced the standard deviation of 1.20 cm in Fig. 8f. The combine method phase in Fig. 8g helps to reduce the standard deviation of 1.20 cm with the 28.05% quality in Fig. 8h.

3.2. Quality Assessment of Atmospheric Correction

The performance of atmospheric corrections is calculated and presented with a plot of quality (Q: in

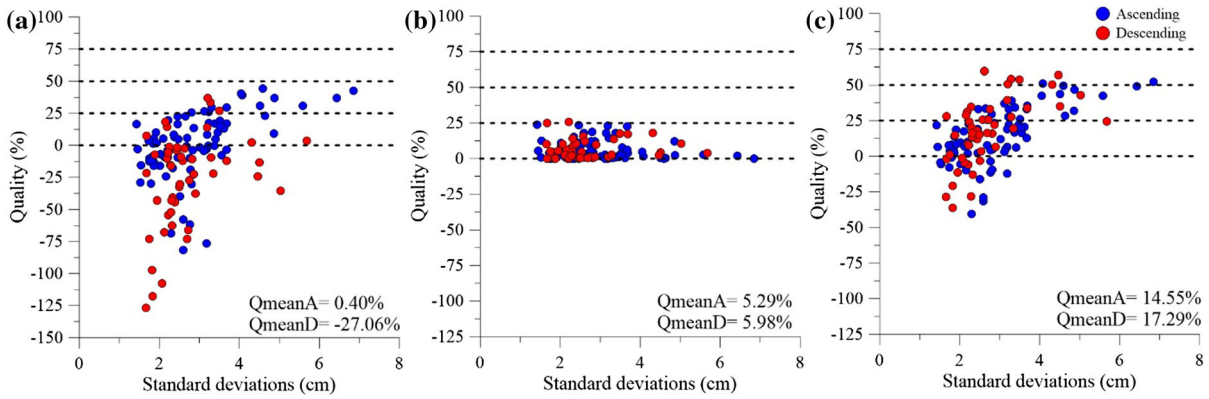

Figure 9
Quality assessment of the atmospheric corrections method: the reduction of the standard deviations after corrections (in percent) as a function of the initial standard deviations using **a** only GACOS weather-model, **b** phase-elevation linear model and **c** combined method (ascending (blue) and descending (red) interferograms with mean quality values of ascending and descending interferograms)

per cent) with standard deviations of uncorrected interferograms in Fig. 9. Negative values mean the correction increase the standard deviation of interferogram and overcorrected the interferogram. In Fig. 9a, it is seen that GACOS weather-model method corrected the interferograms which have the high atmospheric signals ($\sigma_i > 2$ cm) better than the low atmospheric signals. In total, 48.71% of the ascending and 81.25% of descending interferograms were overcorrected ($Q < 0$); 34.61% of the ascending and 12.5% of the descending interferograms had $0 < Q < 0.25$; 16.66% of ascending and 6.25% of descending interferograms had $0.25 < Q < 0.50$. In Fig. 9b, it is shown that the phase-elevation method corrected the interferograms which have lower atmospheric signals ($\sigma_i < 2$ cm) better than those with significant atmospheric signals. 78.20% of ascending and 75% of descending interferograms had $0 < Q < 0.10$; 21.79% of ascending and 22.91% of descending interferograms had $0.10 < Q < 0.25$. Only one interferogram had a Q factor above 25% (descending). In Fig. 9c shows that the combined method reduces the numbers of overcorrected interferogram ($Q < 0$). 53.84% of ascending and 39.58% of descending interferograms had $0 < Q < 0.25$; 25.64% of ascending and 25% of descending interferograms had $0.25 < Q < 0.50$ and 2.56% of ascending and 12.5% of descending interferograms had $0.50 < Q < 0.75$. The mean quality values for ascending (QmeanA) and descending interferograms (QmeanD) were obtained as 0.40% and − 27.56% after GACOS correction, 5.29% and 5.98% after phase-elevation linear method correction, 14.55% and 17.29% after the combined method respectively.

4. Results

A least-squares inversion method was applied to the 78 ascending and 57 descending interferograms and 29 and 23 number of cumulative displacement maps were obtained for ascending and descending respectively after inversion of corrected interferograms. Then, time-series of A, B, C and D points are given to compare after correction and without correction. The standard deviation of each point is plotted as error bars and each value is the mean value of neighbour 10 × 10 pixel. In Fig. 10, the time-series of ascending interferograms are shown before and after correction. The cumulative displacement values of all points are synchronized without correction result in Fig. 10a and the values vary between − 16 and 4 cm. After the correction, the values change between almost − 6 and 6 cm in Fig. 10b. The correction reduced temporal standard deviation on all of the points. Highest temporal standard deviation is in the C point which is stated on the Karaada as 3.97 cm after correction and 2.18 cm without correction probably due to its proximity to the earthquake epicentre. The temporal standard

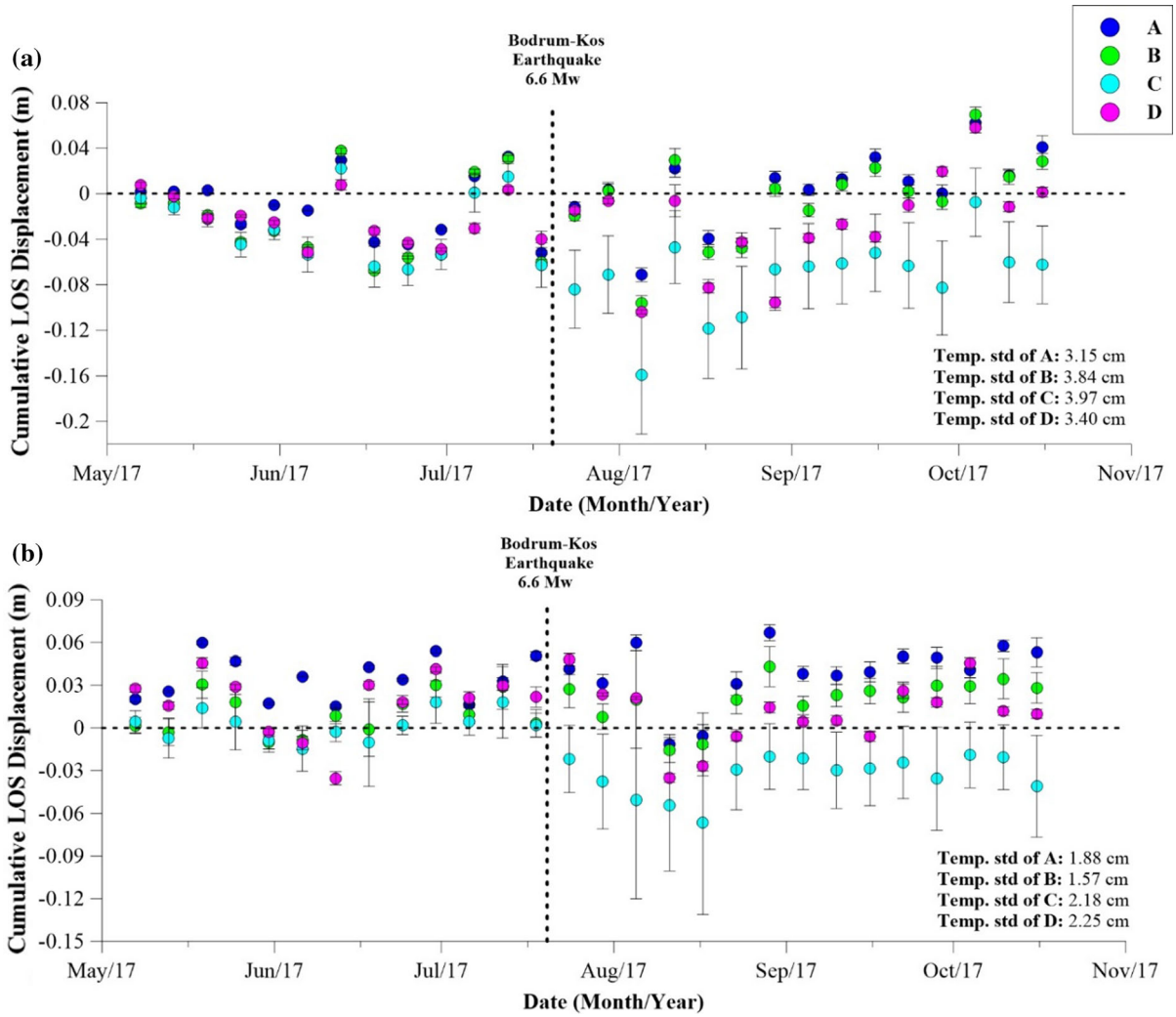

Figure 10
Time series of the ascending interferograms at A, B, C and D (in Fig. 1) with error bars of each point and temporal standard deviations between May–November **a** without correction, **b** after least-squares inversion of interferograms

deviation of A point which is located on the Kos island is obtained as 3.15 cm without correction and the value reduced as 1.88 cm after correction. The temporal standard deviation of B point which is located on the coast of Bodrum is obtained without correction and after correction as 3.84 cm and 1.57 cm respectively. The temporal standard deviation of D point which is located on Rhodes island is obtained without correction and after correction as 3.40 cm and 2.25 cm respectively.

In Fig. 11, time-series of descending interferograms are shown for A, B, C and D points before and after correction. The cumulative displacement values of A, B, C and D points show ~ -24 to ~ -4 cm displacement without correction in Fig. 11a. After the correction, the displacement values of points change between almost -6 to 4 cm in Fig. 11b. The correction reduced temporal standard deviation on all of the points. Highest temporal standard deviation is in the C point which is stated on the Karaada as 4.43 cm after correction and 1.65 cm without correction probably due to its proximity to the earthquake epicentre. The temporal standard deviation of A point which is located on the Kos island is obtained as

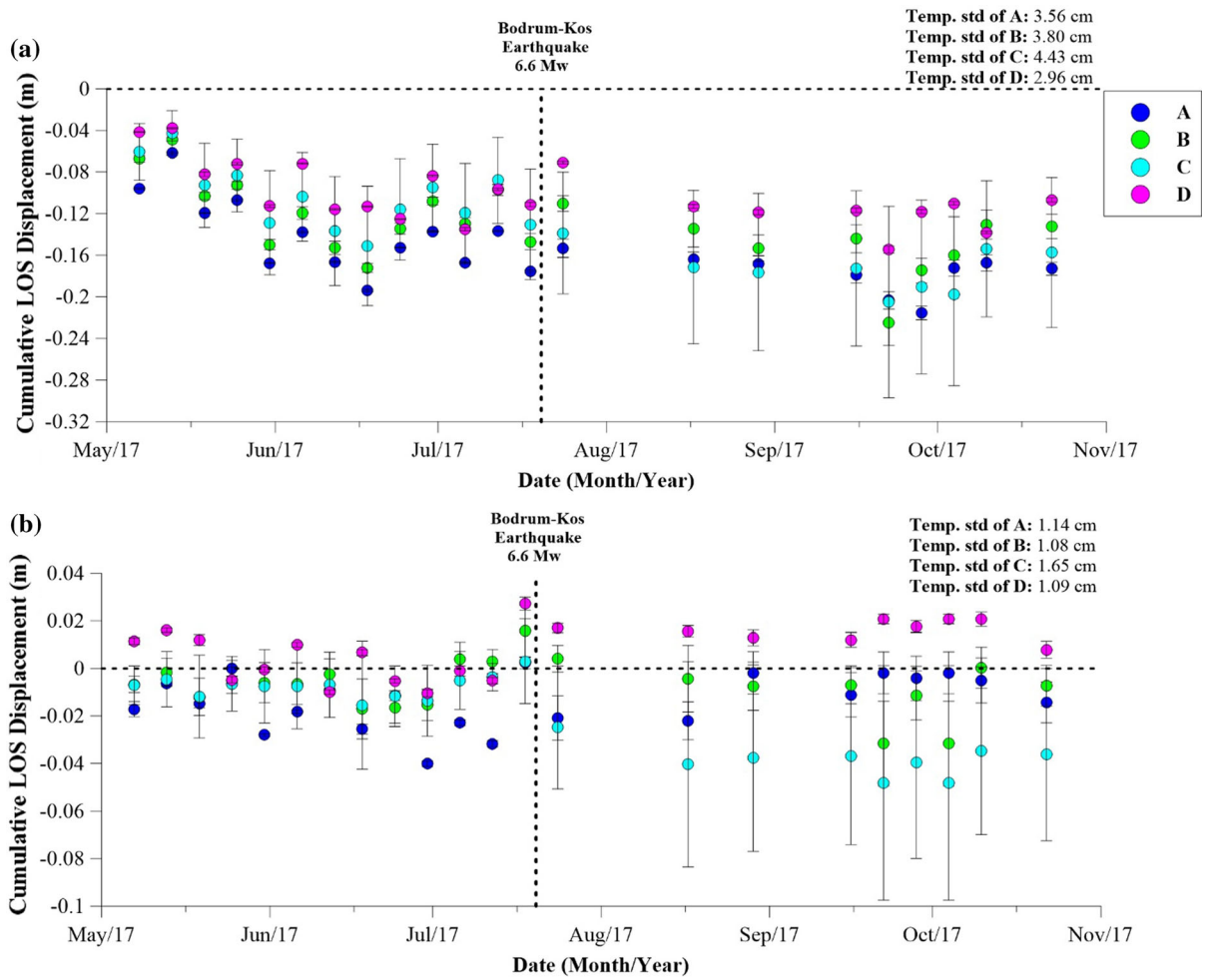

Figure 11
Time series of the descending interferograms at A, B, C and D (in Fig. 1) with error bars of each point and temporal standard deviations between May–November **a** without correction, **b** after least-squares inversion of interferograms

3.56 cm without correction and the value reduced as 1.14 cm after correction. The temporal standard deviation of B point which is located on the coast of Bodrum is obtained without correction and after correction as 3.80 cm and 1.08 cm respectively. The temporal standard deviation of D point which is located on Rhodes island is obtained without correction and after correction as 2.96 cm and 1.09 cm respectively.

Figures 12 and 13 show the cumulative LOS displacement maps for ascending interferograms before and after correction between May and October 2017. t_0 dates as 01 May 2017 for ascending and descending cumulative LOS displacement maps. The total cumulative LOS displacement values vary between − 20 and 20 cm. The displacement values change between − 10 and 10 cm on Karaada before correction and earthquake but displacement could not be recognized on Karaada after correction and before the earthquake. Almost 10 cm subsidence was observed after the earthquake on Karaada after correction.

Figures 14 and 15 show the cumulative LOS displacement maps for descending interferograms before and after correction between May and October 2017. The displacement values change between − 20 and − 10 cm all over the study area before correction but displacement could not be recognized on Karaada

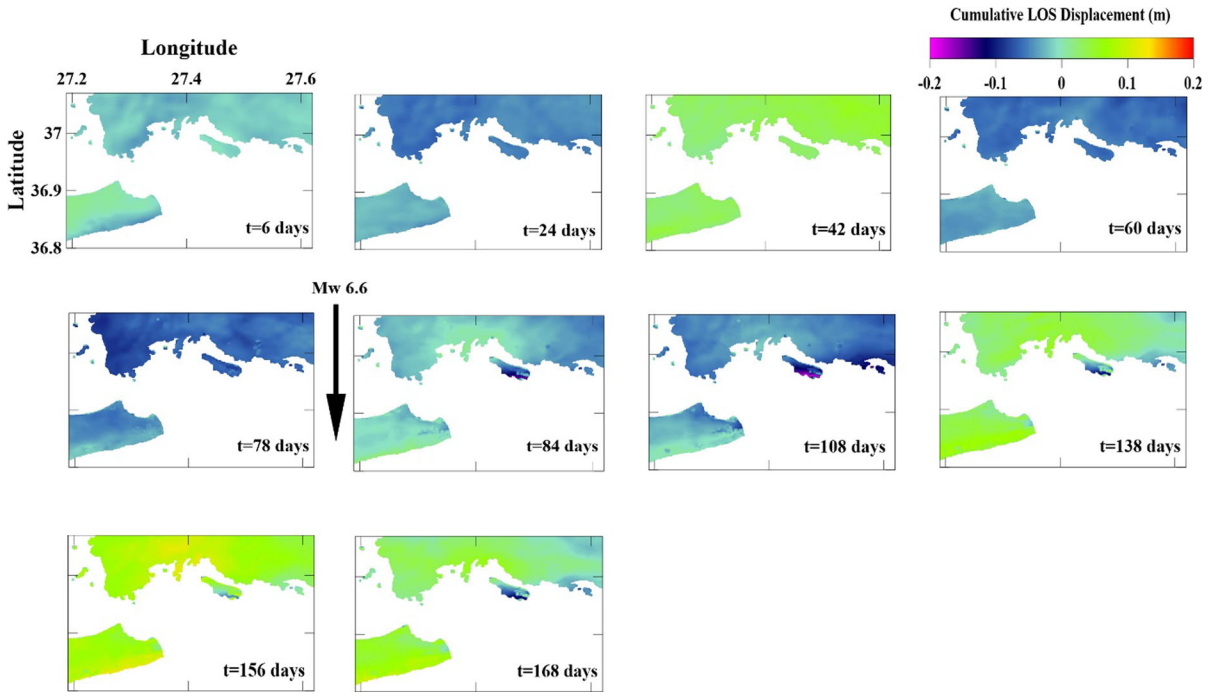

Figure 12
Cumulative LOS displacement maps of ascending interferograms before correction (t_0 = 20170501)

after correction and before the earthquake. Almost 10 cm subsidence was observed after the earthquake on Karaada likewise ascending results. In addition, all cumulative LOS displacement pixel values of Karaada were compared before and after correction in Fig. 16.

The LOS velocity maps for ascending and descending interferograms were calculated using the equation in Le Mouélic et al. (2005) paper before and after correction. It is seen that atmospheric corrections reduce the high positive signals over the Bodrum and coast of Kos island for ascending results (Fig. 17a and c). Also, descending result show high negative signal all over the study area before correction and the atmospheric corrections reduce the signals almost all over the area after correction (Fig. 17b and d). 20 cm subsidence was observed on the Karaada from ascending and descending results in the LOS velocity maps after correction.

d_e and d_u components were calculated after LOS velocity maps and the values obtained as − 20 to 20 cm (Fig. 18). Then, the black rectangle area in which the earthquake occurred was zoomed to see displacement over Karaada and Bodrum coast (Fig. 19). It is seen that coast of Bodrum, Karaada and Kos island move to the west as ∼ 10–20 cm in Fig. 19a and ∼ 20 cm subsidence was observed in the southern part of Karaada in Fig. 19b.

5. Discussions and Conclusions

As a result of this study, it can be said easily atmospheric corrections were applied on InSAR data successfully when taking into account the standard deviation values. In the quality assessment results, the mean quality of GACOS correction is obtained as 0.40% and − 27.06%, phase-elevation correction as 5.29% and 5.98% combined method as 14.55% and 17.29% for ascending and descending respectively (Fig. 9). It is obviously seen that combination of GACOS, phase-elevation and detrend methods reduced the number of overcorrected interferograms after GACOS correction.

Time-series results of A, B, C and D points show that all the points are synchronized till to the

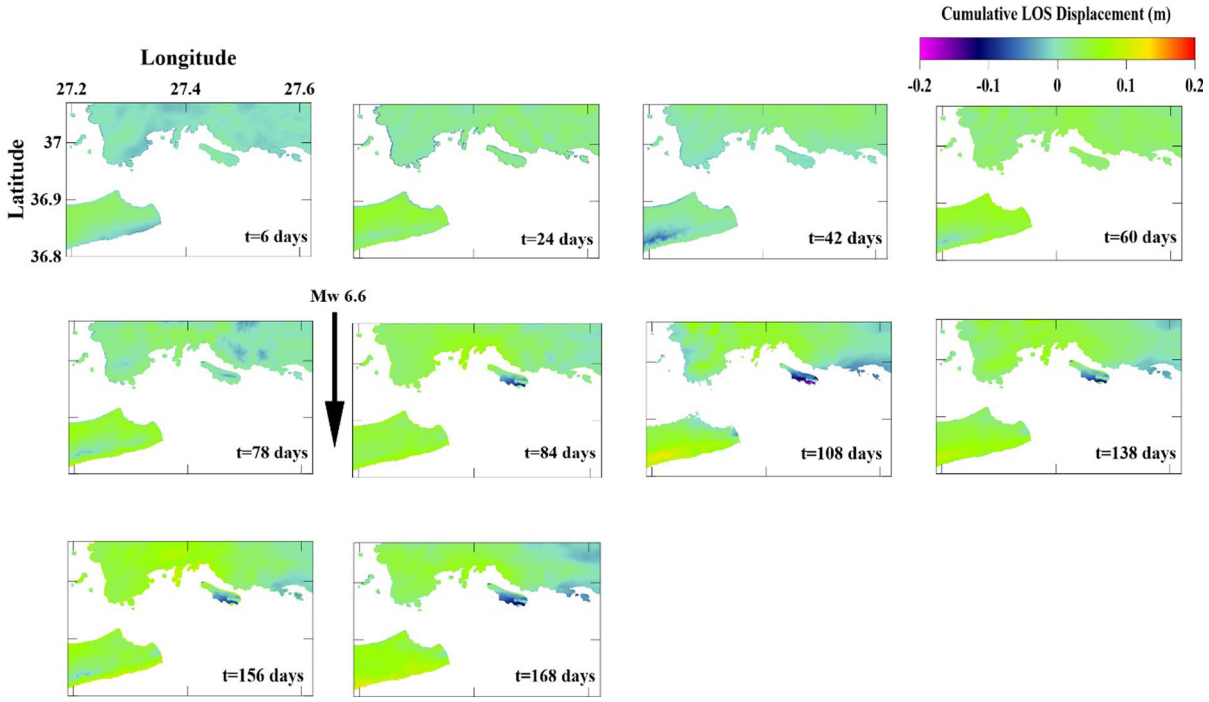

Figure 13
Cumulative LOS displacement maps of ascending interferograms after correction (t_0 = 20170501)

earthquake. After the earthquake, significant subsidence was recognized on the C point which is on the Karaada from inversion of corrected ascending and descending interferograms (Figs. 10 and 11). Atmospheric corrections reduced − 16 cm displacement values in the uncorrected ascending time series result as − 6 cm after correction (Fig. 10). Moreover, atmospheric corrections help to reduce − 20 cm displacement values as − 6 cm after correction of descending interferograms (Fig. 11). When the cumulative LOS displacement maps were examined, it is seen that the values are so fluctuation like subsidence and uplift on Karaada after 6 days without known any event bigger than Mw 6 before correction but Karaada is so stable till to earthquake date after the inversion of corrected ascending interferograms (Figs. 12 and 13). Likewise, only subsidence values were observed before and after the earthquake from the inversion of uncorrected descending interferogram (Fig. 14). Presented corrections reduce the atmospheric effects and cumulative LOS displacement maps of corrected descending interferograms were calculated similarly to correct ascending interferograms (Fig. 15). LOS displacement ranges between + 2.8 cm to − 16.8 cm for ascending interferograms in the InSAR study of Ganas et al. (2018). Moreover, Karasozen et al. (2018) showed 16 cm of subsidence in their study. In this study, ∼ 13–14 cm subsidence was obtained on the Karaada after correction and ∼ 17–18 cm subsidence was obtained without correction (Fig. 16).

Atmospheric corrections help to reduce high positive signals over the Bodrum and coast of Kos island for ascending results and high negative signal all over the study area for descending results (Fig. 17). 20 cm subsidence was observed on the Karaada from ascending and descending results in the LOS velocity maps after correction. d_e and d_u components were calculated after LOS velocity maps and the values obtained as − 20 to 20 cm (Fig. 18). Figure 18 shows that the surrounding of Bodrum, Karaada and Kos island moves west part as 10 cm. Furthermore, coast of Bodrum, Karaada and Kos island move to the west as ∼ 10–20 cm in Fig. 19a

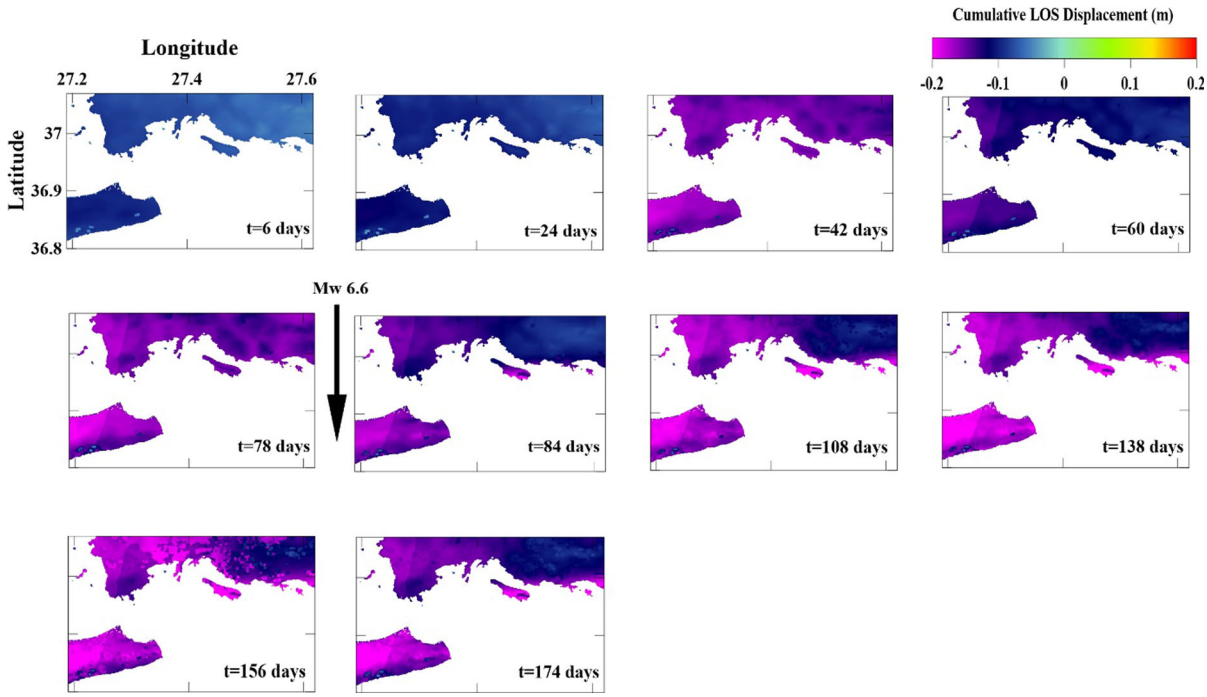

Figure 14
Cumulative LOS displacement maps of descending interferograms before correction (t_0 = 20170501)

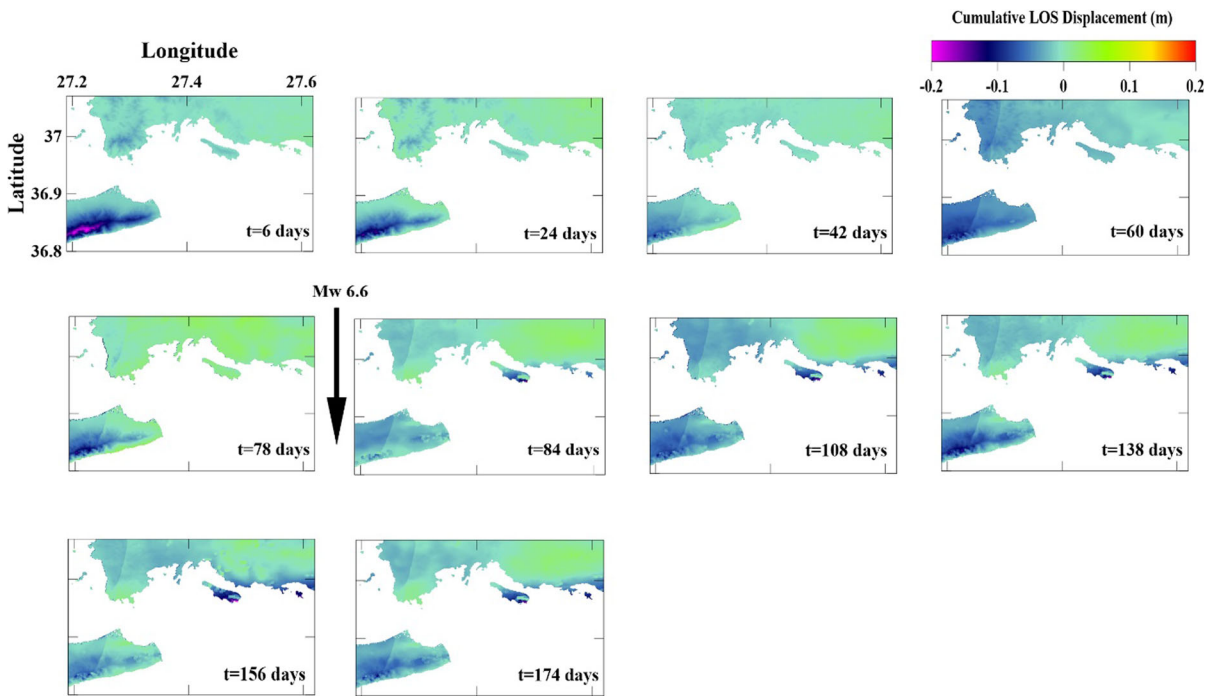

Figure 15
Cumulative LOS displacement maps of descending interferograms after correction (t_0 = 20170501)

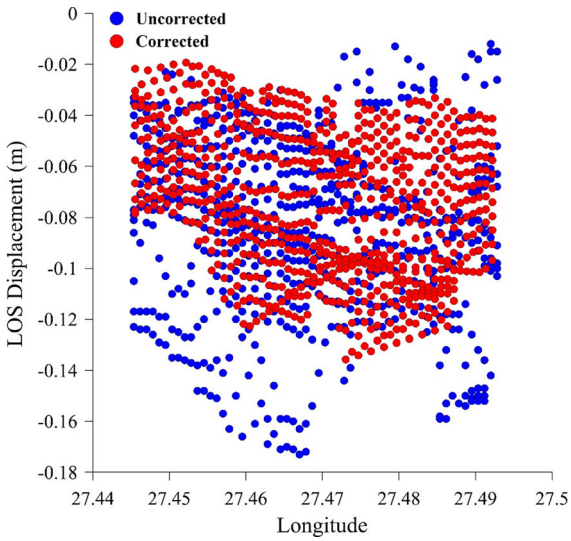

Figure 16
LOS displacement result of all pixels on Karaada after the earthquake with and without correction

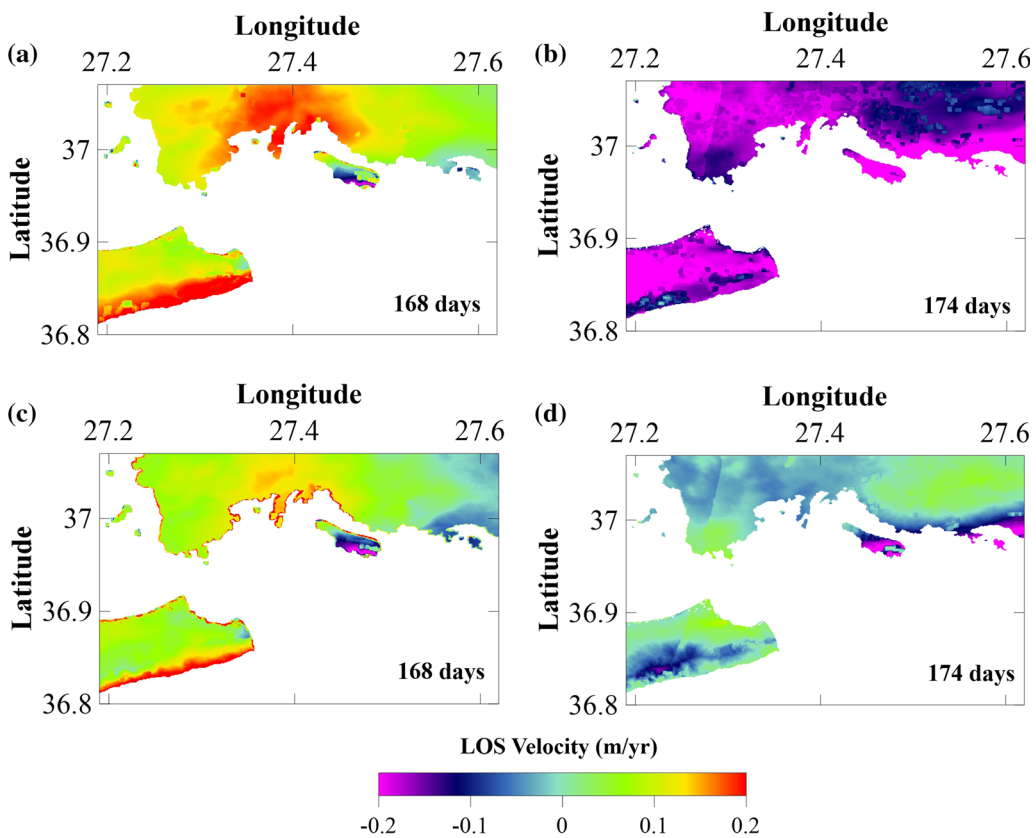

Figure 17
The LOS velocity maps of ascending and descending interferograms calculated from Le Mouélic et al. (2005) **a** ascending LOS velocity map before correction, **b** descending LOS velocity map before correction, **c** ascending LOS velocity map after correction, **d** descending LOS velocity map after correction

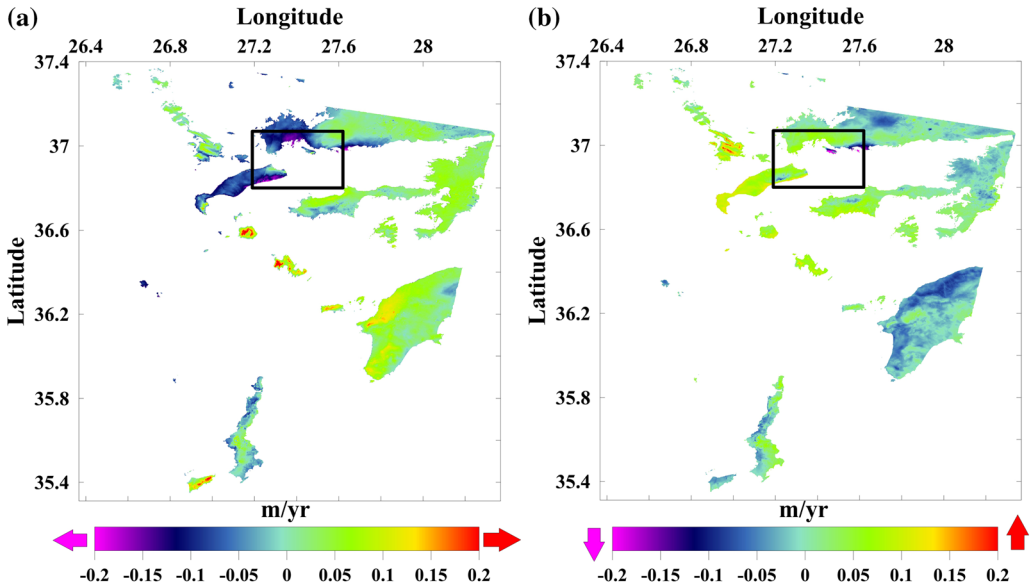

Figure 18
d_e and d_u components **a** d_e component, **b** d_u component

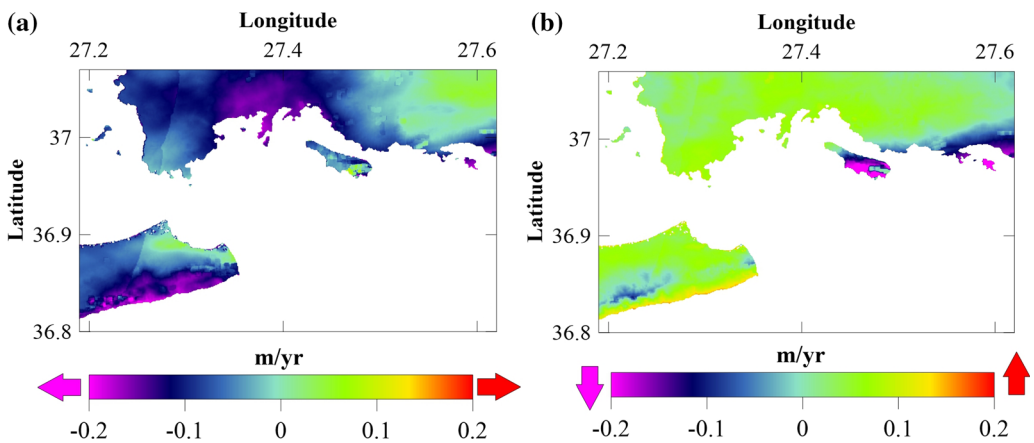

Figure 19
Zoomed d_e and d_u components **a** d_e component, **b** d_u component

and $\sim$ 20 cm subsidence was observed in the southern part of Karaada after zoomed the black rectangle area in Fig. 19b.

Acknowledgements

I would like to thank Dr. Fabien Albino and Prof. Dr. Juliet Biggs for their kindly assistance with atmospheric corrections. Besides, I would like to thank the reviewers and the editor for their helpful comments on the paper. Also, I would like to thank COMET-LiCS Sentinel-1 Sentinel Portal which contains modified Copernicus Sentinel data [2017] analysed by the Centre for the Observation and Modelling of Earthquakes, Volcanoes and Tectonics (COMET). LiCSAR uses JASMIN, the UK's

collaborative data analysis environment (https://jasmin.ac.uk).

Publisher's Note Springer Nature remains neutral with regard to jurisdictional claims in published maps and institutional affiliations.

References

Albino, F., Biggs, J., & Syahbana, D. K. (2019). Dyke intrusion between neighbouring arc volcanoes responsible for 2017 pre-eruptive seismic swarm at Agung. *Nature Communications, 10*(1), 748.

Albino, F., Biggs, J., Yu, C., & Li, Z. (2020). Automated methods for detecting volcanic deformation using Sentinel-1InSAR time series illustrated by the 2017–2018 unrest at Agung, Indonesia. *Journal of Geophysical Research: Solid Earth*. https://doi.org/10.1029/2019JB017908.

Biggs, J., Bergman, E., Emmerson, B., Funning, G. J., Jackson, J., Parsons, B., & Wright, T. J. (2006). Fault identification for buried strike-slip earthquakes using InSAR: The 1994 and 2004 Al Hoceima, Morocco earthquakes. *Geophysical Journal International, 166*(3), 1347–1362.

Biggs, J., Burgmann, R., Freymueller, J. T., Lu, Z., Parsons, B., Ryder, I., & Wright, T. (2009). The postseismic response to the 2002 M 7.9 Denali Fault earthquake: Constraints from InSAR 2003–2005. *Geophysical Journal International, 176*(2), 353–367.

Biggs, J., Robinson, D. P., & Dixon, T. H. (2009). The 2007 Pisco, Peru, earthquake (M 8.0): Seismology and geodesy. *Geophysical Journal International, 176*(3), 657–669.

Bos, A. G., Usai, S., & Spakman, W. (2004). A joint analysis of GPS motions and InSAR to infer the coseismic surface deformation of the Izmit, Turkey earthquake. *Geophysical Journal International, 158*(3), 849–863.

Burgmann, R., Ayhan, M. E., Fielding, E. J., Wright, T. J., McClusky, S., Aktug, B., & Turkezer, A. (2002). Deformation during the 12 November 1999 Duzce, Turkey, earthquake, from GPS and InSAR data. *Bulletin of the Seismological Society of America, 92*(1), 161–171.

Chlieh, M., De Chabalier, J. B., Ruegg, J. C., Armijo, R., Dmowska, R., Campos, J., & Feigl, K. L. (2004). Crustal deformation and fault slip during the seismic cycle in the North Chile subduction zone, from GPS and InSAR observations. *Geophysical Journal International, 158*(2), 695–711.

Cordrie, L., Gailler, A., Heinrich, P., Hébert, H., & Schindelé, F. (2018). Tsunami modeling of the 20th July 2017 Mw 6.6 earthquake in the Aegean Sea. In *EGU General Assembly Conference Abstracts*, *20*, 15114.

Delouis, B., Lundgren, P., Salichon, J., & Giardini, D. (2000). Joint inversion of InSAR and teleseismic data for the slip history of the 1999 Izmit (Turkey) earthquake. *Geophysical Research Letters, 27*(20), 3389–3392.

Dewey, J. F. (1988). Extensional collapse of orogens. *Tectonics, 7*(6), 1123–1139.

Dewey, J. F., & Şengör, A. M. C. (1979). Aegean and surrounding regions: complex multi-plate and continuum tectonics in a convergent zone. *Geological Society of America Bulletin, 90*(1), 89–92.

Dogan, U., Demir, D. Ö., Çakir, Z., Ergintav, S., Ozener, H., Akoğlu, A. M., & Reilinger, R. (2014). Postseismic deformation following the Mw 7.2, 23 October 2011 Van earthquake (Turkey): Evidence for aseismic fault reactivation. *Geophysical Research Letters, 41*(7), 2334–2341.

Doin, M. P., Lasserre, C., Peltzer, G., Cavalié, O., & Doubre, C. (2009). Corrections of stratified tropospheric delays in SAR interferometry: Validation with global atmospheric models. *Journal of Applied Geophysics, 69*(1), 35–50.

Elliott, J. R., Copley, A. C., Holley, R., Scharer, K., & Parsons, B. (2013). The 2011 Mw 7.1 Van (eastern Turkey) earthquake. *Journal of Geophysical Research Solid Earth, 118*(4), 1619–1637.

Ergintav, S., McClusky, S., Hearn, E., Reilinger, R., Cakmak, R., Herring, T., & Tari, E. (2009). Seven years of postseismic deformation following the 1999, M= 7.4 and M= 7.2, Izmit-Düzce, Turkey earthquake sequence. *Journal of Geophysical Research Solid Earth, 114*(B7), 1–19.

Feng, W., Li, Z., Hoey, T., Zhang, Y., Wang, R., Samsonov, S., & Xu, Z. (2014). Patterns and mechanisms of coseismic and post-seismic slips of the 2011 MW 7.1 Van (Turkey) earthquake revealed by multi-platform synthetic aperture radar interferometry. *Tectonophysics, 632,* 188–198.

Fielding, E. J., Lundgren, P. R., Taymaz, T., Yolsal-Çevikbilen, S., & Owen, S. E. (2013). Fault-slip source models for the 2011 M 7.1 Van earthquake in Turkey from SAR interferometry, pixel offset tracking, GPS, and seismic waveform analysis. *Seismological Research Letters, 84*(4), 579–593.

Ganas, A., Elias, P., Kapetanidis, V., Valkaniotis, S., Briole, P., Kassaras, I., & Moshou, A. (2018). The July 20, 2017 M6. 6 Kos-Bodrum earthquake: seismic and geodetic evidence for a north-dipping, normal fault at the western end of the Gulf of Gökova, SE Aegean Sea. In *EGU General Assembly Conference Abstracts, 20*, 9262.

González, P. J., Walters, R. J., Hatton, E. L., Spaans, K., McDougall, A., Hooper, A. J., & Wright, T. J. (2016). LiCSAR: Tools for automated generation of Sentinel-1 frame interferograms. Ion *AGU Fall Meeting*.

Hamiel, Y., & Fialko, Y. (2007). Structure and mechanical properties of faults in the North Anatolian Fault system from InSAR observations of coseismic deformation due to the 1999 Izmit (Turkey) earthquake. *Journal of Geophysical Research Solid Earth, 112*(B7), 1–12.

Hanssen, R. F. (2001). *Radar interferometry: Data interpretation and error analysis*. Dordrecht: Kluwer Academic Publishers.

Hooper, A., Wright, T. J., Spaans, K., Elliott, J., Weiss, J. R., Bagnardi, M., & McDougall, A. (2018). Global monitoring of fault zones and volcanoes with Sentinel-1. In *IGARSS 2018–2018 IEEE International Geoscience and Remote Sensing Symposium* (pp. 1566–1568).

Jolivet, R., Grandin, R., Lasserre, C., Doin, M. P., & Peltzer, G. (2011). Systematic InSAR tropospheric phase delay corrections from global meteorological reanalysis data. *Geophysical Research Letters, 38*(17), 1–6.

Kaneko, Y., Fialko, Y., Sandwell, D. T., Tong, X., & Furuya, M. (2013). Interseismic deformation and creep along the central section of the North Anatolian fault (Turkey): InSAR observations and implications for rate-and-state friction properties. *Journal of Geophysical Research Solid Earth, 118*(1), 316–331.

Karasözen, E., Nissen, E., Büyükakpınar, P., Cambaz, M. D., Kahraman, M., Kalkan, E., & Özacar, A. A. (2018). The 2017 July 20 M w 6.6 Bodrum-Kos earthquake illuminates active faulting in the Gulf of Gökova, SW Turkey. *Geophysical Journal International, 214*(1), 185–199.

Konca, A. O., Guvercin, S. E., Ozarpaci, S., Ozdemir, A., Funning, G. J., Dogan, U., & Reilinger, R. (2019). Slip distribution of the 2017 M w6. 6 Bodrum-Kos earthquake: resolving the ambiguity of fault geometry. *Geophysical Journal International, 219*(2), 911–923.

Lawrence, B. N., Bennett, V. L., Churchill, J., Juckes, M., Kershaw, P., Pascoe, S., et al. (2013). *Storing and manipulating environmental big data with JASMIN*. San Francisco: IEEE Big Data.

Le Mouélic, S., Raucoules, D., Carnec, C., & King, C. (2005). A least squares adjustment of multi-temporal InSAR data. *Photogrammetric Engineering and Remote Sensing, 71*(2), 197–204.

Le Pichon, X., & Angelier, J. (1979). The Hellenic arc and trench system: A key to the evolution of eastern Mediterranean area. *Tectonophysics, 60,* 1–42.

Michel, R., & Avouac, J. P. (2002). Deformation due to the 17 August 1999 Izmit, Turkey, earthquake measured from SPOT images. *Journal of Geophysical Research Solid Earth, 107*(B4), 1–8.

Morishita, Y., Lazecky, M., Wright, T. J., Weiss, J. R., Elliott, J. R., & Hooper, A. (2020). LiCSBAS: An open-source InSAR time series analysis package integrated with the LiCSAR automated Sentinel-1 InSAR processor. *Remote Sensing, 12,* 424.

Motagh, M., Schurr, B., Anderssohn, J., Cailleau, B., Walter, T. R., Wang, R., & Villotte, J. P. (2010). Subduction earthquake deformation associated with 14 November 2007, Mw 7.8 Tocopilla earthquake in Chile: Results from InSAR and aftershocks. *Tectonophysics, 490*(1–2), 60–68.

Reilinger, R. E., Ergintav, S., Burgmann, R., McClusky, S., Lenk, O., Barka, A., & Aktug, B. (2000). Coseismic and postseismic fault slip for the 17 August 1999, M= 7.5, Izmit, Turkey earthquake. *Science, 289*(5484), 1519–1524.

Sengör, A. M. C., Satir, M., & Akkök, R. (1984). Timing of tectonic events in the Menderes Massif, western Turkey: Implications for tectonic evolution and evidence for Pan-African basement in Turkey. *Tectonics, 3*(7), 693–707.

Seyitoğlu, G., & Scott, B. C. (1991). Late Cenozoic crustal extension and basin formation in west Turkey. *Geological Magazine, 128,* 155–221.

Simons, M., Fialko, Y., & Rivera, L. (2002). Coseismic deformation from the 1999 M w 7.1 Hector Mine, California, earthquake as inferred from InSAR and GPS observations. *Bulletin of the Seismological Society of America, 92*(4), 1390–1402.

Tiryakioğlu, İ, Aktuğ, B., Yiğit, C. Ö., Yavaşoğlu, H. H., Sözbilir, H., Özkaymak, Ç., & Özener, H. (2018). Slip distribution and source parameters of the 20 July 2017 Bodrum-Kos earthquake (Mw6. 6) from GPS observations. *Geodinamica Acta, 30*(1), 1–14.

Usai, S. (2003). A least squares database approach for SAR interferometric data. *IEEE Transactions on Geoscience and Remote Sensing, 41*(4), 753–760.

Wang, C., Ding, X., Li, Q., Shan, X., Zhu, W., Guo, B., & Liu, P. (2015). Coseismic and postseismic slip models of the 2011 Van earthquake, Turkey, from InSAR, offset-tracking, MAI, and GPS observations. *Journal of Geodynamics, 91,* 39–50.

Werner, C., Wegmüller, U., Strozzi, T., & Wiesmann, A. (2000). Gamma SAR and interferometric processing software. In *Proceedings of the ERS-ENVISAT symposium*, Gothenburg, Sweden, 1620.

Wright, T., Fielding, E., & Parsons, B. (2001). Triggered slip: Observations of the 17 August 1999 Izmit (Turkey) earthquake using radar interferometry. *Geophysical Research Letters, 28*(6), 1079–1082.

Wright, T. J., Parsons, B. E., & Lu, Z. (2004). Toward mapping surface deformation in three dimensions using InSAR. *Geophysical Research Letters, 31*(1), 1–5.

Yu, C., Penna, N. T., & Li, Z. (2017). Generation of real-time mode high-resolution water vapor fields from GPS observations. *Journal of Geophysical Research Atmospheres, 122*(3), 2008–2025.

Yu, C., Li, Z., Penna, N. T., & Crippa, P. (2018). Generic atmospheric correction model for Interferometric Synthetic Aperture Radar observations. *Journal of Geophysical Research Solid Earth, 123*(10), 9202–9222.

Yu, C., Li, Z., & Penna, N. T. (2018). Interferometric synthetic aperture radar atmospheric correction using a GPS-based iterative tropospheric decomposition model. *Remote Sensing of Environment, 204,* 109–121.

(Received July 20, 2020, revised September 30, 2020, accepted October 10, 2020, Published online October 22, 2020)